



Numerical simulation of intense-beam experiments at LLNL and LBNL

S.M. Lund^{a,*}, J.J. Barnard^a, G.D. Craig^a, A. Friedman^a, D.P. Grote^a, H.S. Hopkins^a,
T.C. Sangster^a, W.M. Sharp^a, S. Eylon^b, T.J. Fessenden^b, E. Henestroza^b, S. Yu^b, I. Haber^c

^a *Lawrence Livermore National Laboratory, University of California, PO Box 808, L-440, Livermore, CA 94550, USA*

^b *Lawrence Berkeley National Laboratory, University of California, USA*

^c *Plasma Physics Division, Naval Research Laboratory, California, USA*

Abstract

We present intense-beam simulations with the WARP code that are being carried out in support of the Heavy-Ion Fusion experimental programs at Lawrence Livermore National Laboratory (LLNL) and Lawrence Berkeley National Laboratory (LBNL). The WARP code is an electrostatic particle-in-cell code with an extensive hierarchy of simulation capabilities. Two experiments are analyzed. First, simulations are presented on an 80 keV, 2 mA K^+ bent transport channel at LLNL that employs an alternating-gradient lattice of magnetic quadrupoles for beam focusing and electric dipoles for beam bending. Issues on dispersion-induced changes in beam quality on the transition from straight- to bent-lattice sections are explored. The second experiment analyzed is a 2 MeV, 800 mA, driver-scale injector and matching section at LBNL that is based on a K^+ source and an alternating-gradient lattice of electrostatic quadrupoles biased to accelerate, focus, and match the beam. Issues on beam quality, space-charge waves, and beam hollowing are explored. Published by Elsevier Science B.V.

1. Introduction

In the proposed induction-accelerator based drivers for Heavy-Ion Fusion (HIF), the beams are strongly space-charge dominated and behave as collisionless, nonneutral plasmas confined and accelerated by applied electric and magnetic fields [1–3]. In this regime, methods of simulation employing a self-consistent field description are essential in evaluating possible deleterious effects of

nonlinear space-charge forces and collective instabilities. Numerical simulations that combine the self-consistent particle-in-cell (PIC) method from plasma physics with features of conventional accelerator codes for weak space-charge forces have become an accepted tool for the analysis of these beams [1–6].

The electrostatic WARP code [4], developed at LLNL, is a well benchmarked hybrid PIC/accelerator code optimized for studies on induction-based drivers for HIF. WARP has been used to simulate a wide variety of problems in accelerators for HIF, ranging from the source to the final focus optics [1–6]. An extensive hierarchy of WARP modeling

*Corresponding author. Tel. +1 510 423 4463; fax: +1 510 423 2664.

capabilities enables accelerator concepts and theory to be tested under varying degrees of idealization, thereby providing insight on issues in both physics and numerical modeling. WARP has also been valuable in the design and evaluation of experimental hardware [2–6]. Extensive code diagnostics coupled with the capability of simulating high levels of model detail make WARP a valuable tool for experimental support. WARP is presently used to simulate both a wide range of experiments and a wide range of processes within individual experiments [3,6].

In this article, we highlight WARP simulation capabilities by modeling two intense-beam experiments, one being carried out at LLNL, and the other at LBNL. First, in Section 2, a brief overview of the WARP code is presented. Following this, in Section 3, simulations are presented on a beam-bending experiment at LLNL to explore dispersion-induced changes in beam quality. Then, in Section 4 simulations are presented on an injector experiment at LBNL to explore the evolution of space-charge waves and possible mechanisms of experimentally observed beam hollowing.

2. WARP code for intense beam modeling

An extensive set of simulation tools have been developed at LLNL to model intense ion-beam induction accelerators for applications in HIF [1–3]. These tools range from: simple system codes designed to estimate machine parameters and cost; to envelope codes that rapidly advance second-order moments of the beam to determine beam focusing and acceleration requirements, etc.; to electrostatic and electromagnetic PIC codes of varying dimensionality and levels of modeling detail. In this article, we present applications of the WARP PIC code.

WARP is a flexible, multi-dimensional PIC code that employs “WARPed” coordinates to allow the computational mesh to follow a bent lattice [1–6]. Primary limitations of the code stem from the use of the electrostatic approximation with negligible self-magnetic fields, and a uniform increment computational mesh. WARP is not a single function code, but rather a versatile family of code tools

Table 1
WARP code packages

Package	Variables		Model
WARP3d	x,y,z	v_x,v_y,v_z	3d
WARP _{xy}	x,y	v_x,v_y,v_z	⊥ Slice
WARP _{rz}	r,z	v_r,v_θ,v_z	Axisymmetric
WARPen	a,b	a',b'	Envelope

organized into functional “packages” as summarized in Table 1. These packages range from WARP3d, the most detailed level of modeling, where the three-dimensional (3d) particle coordinates x,y,z and velocities v_x,v_y,v_z are advanced, to WARPen, an envelope package that advances the radii a,b and convergence angles a',b' of an elliptical envelope KV beam with specified emittance. In this paper, we primarily present simulations from the 3d package, WARP3d, and a new transverse (⊥) slice package, WARP_{xy} [3], that includes bends and allows a distribution of axial particle velocities v_z . An interactive Fortran-based interpreter controls both the individual routines making up these packages (fieldsolve, particle movers, etc.) and a common set of diagnostic tools, enabling flexible operation. For example, code for diagnostics can be modified during a run to explore unanticipated effects, and different fieldsolve routines (FFT, SOR, etc., with various boundary conditions) can be employed to test the validity of model approximations in field structure.

Select features of WARP relevant to this study are as follows. First, WARP3d includes a 3d SOR fieldsolver allowing detailed conductor geometry with subgrid resolution. Both four-fold (quadrant) and two-fold (vertical y -plane) ⊥ symmetries can be enforced in simulations of alternating-gradient (AG) transport lattices. Bends are allowed in the in x -plane and applied magnetic or electric fields can be input in multipole or gridded form. Various beam distributions can be initialized, including self-consistent space-charge-limited injection from curved sources, and KV and semi-Gaussian (SG) distributions or various perturbed variants thereof, can be loaded or injected. A simulation of 600 half-lattice periods of a recirculating induction accelerator ($32 \times 16 \times 64$ grid with two-fold symmetry,

75k particles, 50k time-steps) takes approximately 6h on a single processor of a C90 computer. Second, WARPxy is a slice code that includes the features of WARP3d outlined above while providing a more-rapidly running, reduced dimensionality compliment to WARP3d. WARPxy can be initialized with \perp beam slices (including v_z) imported from WARP3d, and the full 3d applied field structure can be input from external sources (i.e., the WARP3d SOR fieldsolver, magnet codes, etc.). The primary limitation of WARPxy is the lack of axial (z) self-field effects. A planned thick-slice generalization should mitigate this limitation. A recirculator problem analogous to the one simulated by WARP3d, when simulated in WARPxy (with a 32×16 grid with two-fold symmetry, 2.5k particles, and 25k axial steps) takes approximately 15 min on the single-processor C90. More extensive reviews of the WARP code have been presented elsewhere [1–6].

3. Simulations of beam-bending experiments at LLNL

LLNL is conducting a scaled recirculator experiment intended to test physics and technology issues associated with an HIF driver concept based on a recirculating induction accelerator. This accelerator was designed to have similar dimensionless beam parameters (perveance, particle phase advances, etc.) to a full-scale driver, while maintaining driver-similar engineering parameters in high-voltage waveforms needed for beam acceleration, bending, compression, axial confinement, and steering. When complete, this small recirculator experiment (14.4m circumference ring) will be able to test, on a small scale, many issues associated with a full-scale recirculating driver. The small recirculator differs from a driver in that it employs, to reduce cost, permanent magnet quadrupoles (PMQs) for AG beam focusing and electric dipoles for beam bending. More details of the small recirculator experiment are contained in Refs. [2,3].

The small recirculator is being assembled as a sequence of progressively complex experiments with the goal of evolving into a fully functional ring while exploring features of the recirculator concept.

Presently, a beam-bending transport experiment (no beam acceleration) is configured which consists of four distinct parts: a diode producing a K^+ beam with energy $\mathcal{E}_b = 80$ keV, current $I = 2$ mA, flat-top pulse duration $\tau = 4 \mu s$, and envelope radius $r_b = 0.52$ cm; followed by an AG matching section with seven electrostatic quadrupoles (ESQs); followed by a straight magnetic transport section (seven half-lattice periods) with AG PMQs; followed by a 45° bent magnetic transport section (five half-lattice periods, each bending the beam centroid 9°) with electric dipoles and AG PMQs. The minimum clear-pipe radius of the lattice (in PMQ apertures) is $r_p = 3.45$ cm. All PMQs [7] are identical, each having a \perp field gradient $|\partial B_y / \partial x| = 916$ G/cm, high field quality, and a 10.4 cm axial length. Likewise, each ESQ in the matching section has a 10.2 cm axial length and is shaped to enhance field quality. Each electric dipole has a 10.7 cm axial length, and is shaped both to enhance field quality and to produce equal particle phase advances in (x – z plane) and out (y – z plane) of the bend plane. The half-lattice periods, L , in each section of the lattice are: $L = 15.2$ cm (first three ESQs) increasing to $L = 30.5$ cm (last four ESQs) in the matching section; $L = 38.1$ cm in the straight magnetic transport section; and $L = 36$ cm in the bent magnetic transport section. Experimental measurements of the beam emerging from the diode obtain, at mid-pulse, normalized rms-edge emittance values $\varepsilon_{nx,ny} = 0.025$ mm mrad. Here and henceforth, for the nonrelativistic beams considered, $\varepsilon_{nx} \simeq (4v_b/c)(\langle x^2 \rangle \langle x'^2 \rangle - \langle xx' \rangle^2)^{1/2}$ (with an analogous expression for ε_{ny}), $v_b = \langle v_z \rangle$ is the mean axial beam velocity ($\mathcal{E}_b = mv_b^2/2$, with m the particle mass), $x' \simeq v_x/v_b$, c is the speed of light in vacuo, and $\langle \dots \rangle$ denotes an average over a \perp beam slice. In the bent transport section, the depressed ($I = 2$ mA) and undepressed ($I \rightarrow 0$) phase advances of \perp particle oscillations per lattice period ($2L$) are $\sigma = 4.3^\circ$ and $\sigma_0 = 77.4^\circ$, respectively. Slit-scanner, gated beam imager, capacitive probe, and traveling-wire diagnostics are available at various locations. Further details of the lattice and diagnostics are presented in Ref. [3].

A key issue in the HIF recirculator concept is the control of beam quality (i.e., minimizing the growth in normalized emittance $\varepsilon_{nx,ny}$) of

space-charge-dominated beams in the presence of waveforms for beam manipulations (acceleration, bending, etc.) that change rapidly as the nonrelativistic beam accelerates. Also, all beams have a finite spread in axial velocity, as measured by the longitudinal thermal velocity $v_{tz} = \langle (v_z - v_b)^2 \rangle^{1/2}$, which can significantly complicate the control of beam quality in a dispersive bent lattice [8]. In a bend, velocity spread induced dispersion is known to lead to emittance growth as a space-charge-dominated beam relaxes to a new “equilibrium” on propagating through lattice transitions. This growth is generally nonreversible due to nonlinear space-charge forces and the magnitude of the growth can be a sensitive function of the dispersion. Sufficient dispersion can necessitate achromatic designs for straight-bent lattice transitions – which is difficult in the presence of strong space-charge [9], and more difficult still with varying lap-to-lap beam energy and/or large imposed head-to-tail beam velocity “tilt” for axial beam compression. Consequently, present recirculator designs favor continuous bends (rings rather than racetracks) to minimize lattice transitions. Nevertheless, straight-bent lattice transitions are a general feature of HIF drivers (with two or more beams on target) and exist even for continuous bend recirculators with straight insertion and extraction sections. Because longitudinal velocity spread is a fundamental issue, it is unfortunate that direct experimental evaluations of the spread generally require difficult, high-resolution measurements. Hence, little is known about the characteristic velocity spread of space-charge-dominated heavy-ion beams. Here we show that the LLNL bend experiment provides a valuable opportunity to indirectly measure the spread by measuring the dispersive growth of the \perp normalized emittances, ε_{nx} and ε_{ny} , as the beam relaxes after the transition from the straight to the bent magnetic transport lattices.

There are several possible sources of axial velocity spread in the LLNL bend experiment and similar long-pulse, intense beam experiments. First, there is an energy spread associated with the heavy-ions launched from a hot-plate cathode source held at thermodynamic temperature T . (T in energy units, with typical $T \sim 0.1 \text{ eV} \Rightarrow \sim 950^\circ\text{C}$ for alumino silicate source loaded

with potassium.) Neglecting instabilities and other nonideal effects, particles accelerated through the diode will have an initial \perp kinetic temperature $T_\perp = (m/2)\langle (v_\perp - \langle v_\perp \rangle)^2 \rangle$ equal to the source temperature T (i.e., $T_\perp = T$), and this temperature will subsequently increase or decrease consistent with any \perp beam envelope compression or expansion away from the source. On the other hand, as presented by Reiser [10], the longitudinal kinetic temperature $T_\parallel = m\langle (v_z - v_b)^2 \rangle = mv_{tz}^2$ of particles accelerated through the diode to energy \mathcal{E}_b will undergo strong accelerative cooling according to $T_\parallel = T^2/2\mathcal{E}_b$, resulting in a small velocity spread with $v_{tz}/v_b = (T/\mathcal{E}_b)/\sqrt{2}$. More significant spread can result from the thermalization of pulser noise (frequency $\gg 1/\tau$) associated with the high-voltage waveforms applied to the diode and any subsequent acceleration gaps. Even with careful engineering, such noise will typically be $\sim 1\%$ of the pulser voltage and will result in each axial slice of the beam having slightly different energy, thereby launching longitudinally propagating waves. These waves can thermalize, leading to increased axial velocity spread [11]. Although such thermalization rates are slow, the large wave-amplitudes could ultimately lead to significant axial velocity spread in a long transport channel. Finally, certain collective modes of space-charge-dominated beams are known to lead to the exchange of thermal energy from the \perp to the longitudinal degrees of freedom [2,3]. Such modes could act rapidly within the diode, where the beam space-charge strength is large. The saturation of such modes is not presently understood, but could, as a worst case, result in a equipartitioned beam with $T_\parallel = T_\perp$. Such a thermal equilibrium beam is the stable, preferred state of nature that the beam is driven to under general considerations [10]. Since the emittance of a thermal equilibrium beam is related to T_\perp by $\varepsilon_{nx} = 2a(T_\perp/m)^{1/2}/c$ (only strictly valid for a round, continuously focused beam with $a = 2\langle x^2 \rangle^{1/2} = r_b$), full equipartitioning would result in a velocity spread with $v_{tz}/v_b = \varepsilon_{nx}/(2av_b/c)$.

For the LLNL bend experiment, accelerative cooling, pulser noise thermalization, and equipartitioning considerations yield a wide possible range of axial velocity spread. The diode has cathode temperature $T \simeq 0.1 \text{ eV}$ and produces an

$\mathcal{E}_b = 80$ keV beam, and therefore ideal accelerative cooling would imply a small lower-bound spread with $v_{tz}/v_b \simeq 8.8 \times 10^{-7}$. The noise of the diode pulser and the rate of noise thermalization has not been measured, but the pulser noise is estimated to be $\sim 5 \times 10^{-3} \mathcal{E}_b$. A complete thermalization of this pulser noise would yield an upper-bound spread with $v_{tz}/v_b = 2.5 \times 10^{-3}$. Intermediate levels of spread would result from full equipartitioning ($T_\perp = T_\parallel$), which for $\varepsilon_{nx} = 0.03$ mm mrad and $r_b = 1.13$ cm (beam entering bend), implies that $v_{tz}/v_b = 6.32 \times 10^{-4}$.

WARP_{xy} slice simulations were carried out to parametrically explore the mid-pulse consequences of beam dispersion over the range of velocity spread $0 \leq v_{tz}/v_b \leq 2.5 \times 10^{-3}$. The bent magnetic transport lattice was periodically extended to form a continuous drifting bend and the applied 3d fields of electric and magnetic elements were input as multipole moments. Both axial fringe and error field components were included. Multipole moments of the ESQs and dipoles were generated from the experimental electrode potentials and a numerical Green function calculated using the SOR field-solver of WARP3d and the detailed electrode structures. Multipole moments of the PMQs were generated from a 3d analytical theory [7]. An initial SG beam was initialized at the diode exit plane with $\mathcal{E}_b = 80$ keV, $I = 2$ mA, $\varepsilon_{nx} = \varepsilon_{ny} = 0.025$ mm mrad, and with beam envelope radius and convergence angle $r_b = 0.542$ cm and $r'_b = 12.5$ mrad, respectively. The initial axial velocity spread v_{tz} was Gaussian distributed and an FFT fieldsolver was used. Typical simulations employed a 128×128 \perp grid with ± 3.5 cm bounds in the x - and y -directions, 40k particles, and an axial (s direction, along reference orbit) particle advance with step size $ds \leq 0.3$ cm. Section transitions correspond to $s = 0$ (diode exit \rightarrow matching section), $s = 1.830$ m (matching \rightarrow straight magnetic transport) and $s = 4.826$ m (straight \rightarrow bent magnetic transport).

The simulated s -evolution of the beam envelope radii $a = 2\langle x^2 \rangle^{1/2}$ and $b = 2\langle y^2 \rangle^{1/2}$ are plotted in Fig. 1. Mid-pulse experimental measurements taken with a gated beam imager at the end of the 45° bend are also plotted, and agree well with the simulations. These measurements are shown as

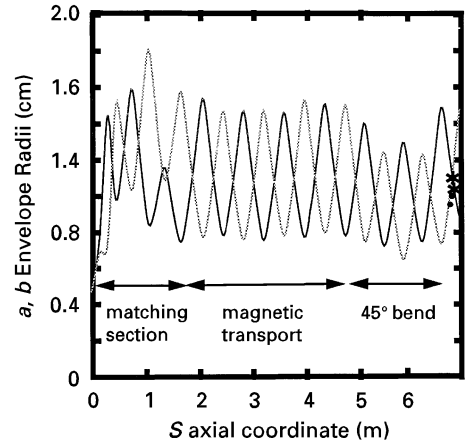


Fig. 1. Axial s -evolution of the beam rms-envelope radii a (black) and b (grey). Experimental measurements in the x - and y -planes are indicated with *s and ●s.

adjacent pairs to illustrate the measured envelope convergence angles. Similar comparisons made at lower beam energy ($\mathcal{E}_b = 75$ keV) and with other diagnostic locations (in matching and straight transport sections) also show good agreement. These results, and the agreement indicated in Fig. 1 after transport through 24 lattice elements, suggest that the applied field structure is accurately modeled by the simulations.

The simulated s -evolution of the \perp normalized emittances $\varepsilon_{nx,ny}$ are plotted in Fig. 2 for $v_{tz}/v_b = 0.132\%$, corresponding to an equipartitioned beam ($T_\perp = T_\parallel$) entering the continuous bend ($s = 4.826$ m) with $\varepsilon_{nx,ny} \simeq 0.03$ mm mrad (increased from the initial value of 0.025 mm mrad at $s = 0$) and $r_b \equiv \sqrt{ab} = 1.13$ cm. Initially, ε_{nx} increases on entering the bend whereas ε_{ny} is unchanged, because the dispersion induces a change in bend strength for ions off design energy, thereby increasing the x' -distribution width in x - x' phase space. Over longer distances, as the beam relaxes to the bent lattice, the bend-plane emittance ε_{nx} undergoes a large-amplitude, damped oscillation in s , whereas the the out-of-bend plane emittance ε_{ny} slowly increases in s as the \perp degrees of freedom (x and y) exchange thermal energy. Results of a continuous-focusing approximation theory [8] of dispersion-induced emittance growth are also plotted in Fig. 2. This theory is constructed on

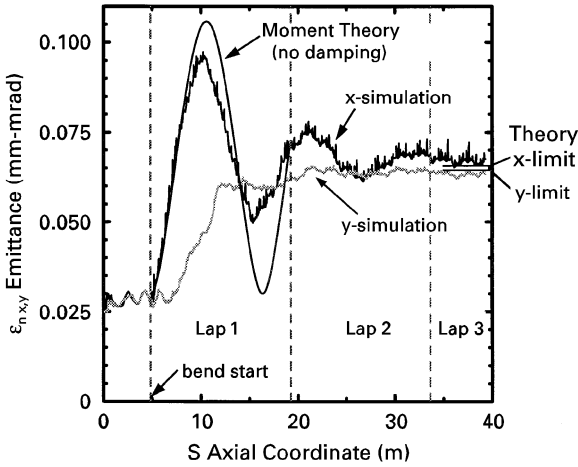


Fig. 2. Axial s -evolution of the normalized beam emittances ε_{nx} and ε_{ny} in a continuous bend, shown for $T_{\perp} = T_{\parallel}$ at the bend start.

a second-order moment truncation (including dispersive v_z moments), and accurately predicts the amplitude and frequency of oscillations in ε_{nx} . The damping in ε_{nx} -oscillations and the rise in ε_{ny} (the theory predicts no initial change in ε_{ny} on entering the bend) are associated with nonlinear space-charge forces outside the scope of the second-order-moment model. However, energy conservation in the continuous focusing approximation can be used to estimate theoretically the limiting values of the emittance growth when the beam fully relaxes to the dispersive bent lattice and the \perp degrees of freedom have equilibrated [8]. These limiting values are plotted in Fig. 2 and agree well with the simulations. Parenthetically, WARPxy results similar to those presented in Fig. 2 agree with mid-pulse simulations with WARP3d, which is well benchmarked for bends.

In Fig. 3, we plot quantities needed to understand how the dispersion-induced oscillation in normalized emittance illustrated in Fig. 2 parametrically changes over the relevant range of v_{tz}/v_b axial velocity spread. Shown are (a) the axial location of the first peak (maximum) in the ε_{nx} -oscillation and a measurement of the point of full beam relaxation to the bent lattice (heuristic, no true AG equilibrium known), both measured in lap location in the recirculator lattice; and (b) the values of

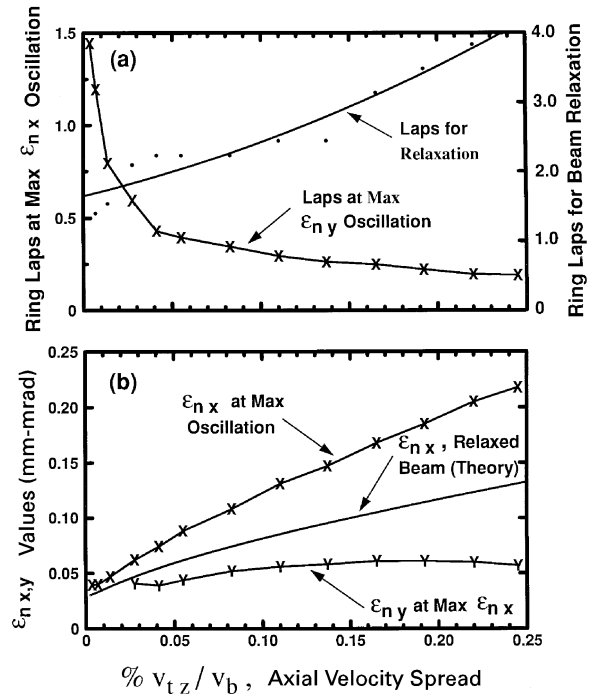


Fig. 3. Change in emittance oscillation features illustrated in Fig. 2 as a function of $\% v_{tz}/v_b$ axial velocity spread.

ε_{nx} and ε_{ny} at maximum ε_{nx} -oscillation, and ε_{nx} for a fully relaxed beam. The relaxed value of ε_{nx} are estimated from theory [8] (agree with simulation) and all other curves are obtained from simulation (points indicated). These curves indicate that both the axial location and the value of the ε_{nx} maximum are sensitive functions of v_{tz}/v_b . Evidently, measurable changes in ε_{nx} should result over a wide range of possible velocity spread, particularly since near-term plans call for the bent lattice to be extended to 135° (0.375 lap) as construction of the ring progresses. Further simulations showed that little enhancement of these measurement possibilities would be obtained by parametric changes in beam energy (\mathcal{E}_b), current (I), and other parameters easily varied in the experiment. Unfortunately, experimental diagnostics were primarily in the insensitive y -plane, and measurements were not directly comparable to the idealized simulation results in Fig. 3. Alignment errors and nonuniformities in the beam emerging from the diode (both being improved)

resulted in large measured increases in ε_{ny} ($\varepsilon_{ny} \sim 0.055$ mm mrad at 45°), thereby complicating the interpretation of any possible dispersion induced changes. Nevertheless, diagnostics are being reconfigured and it is anticipated that careful experimental work can mitigate these problems and/or that the initial nonuniformities in the beam profile can be measured and initialized in the simulations to indirectly bound the actual dispersion. Thus these experiments promise to provide new and fundamentally useful data on the characteristic axial velocity spread of space-charge-dominated beams for HIF.

4. Simulations of ESQ injector experiments at LBNL

Generally speaking, injectors for HIF present difficult technological challenges. The combination of strong space-charge, high voltage gradients with associated breakdown constraints, and limitations in source technology render injector design difficult. These considerations motivated LBNL to lead the development of an ESQ injector option over more conventional architectures based on a Pierce column with multiple axisymmetric apertures. This ESQ injector was constructed at LBNL as part of the planned ILSE/ELISE experiments on linear induction drivers for HIF with the goal of demonstrating a practical injector on a driver relevant scale in energy ($\mathcal{E}_b \sim 2$ MeV), line charge ($\lambda \sim 0.25$ $\mu\text{C}/\text{m}$), and emittance ($\varepsilon_n < 1$ mm mrad) [1–3,12]. The ESQ injector met these goals and is presently being used as an experimental facility [3,12].

The ESQ injector produces a K^+ beam with energy $\mathcal{E}_b = 2$ MeV, current $I = 790$ mA ($\lambda = 0.40$ $\mu\text{C}/\text{m}$), pulse duration $\tau = 1$ μs , and emittance $\varepsilon_{nx,ny} \simeq 0.6$ mm mrad. The system consists of a 2 MV MARX generator powering a 792 keV diode that feeds a 1.208 MeV column of four ESQs, Q1–Q4. The ESQs are constructed from shaped, interdigitated conducting rods attached to conducting endplates with apertures. The rods along the x - and y -planes are connected to alternating endplates and the assembly is biased to produce applied electric fields that accelerate the beam longitudinally while providing \perp beam focusing via an

alternating gradient quadrupole field component. The diode has a 29.5 cm axial length, a 12 cm radius aperture that forms the end-plate of the first ESQ, and a curved, alumino silicate source that is, approximately, a 17 cm diameter interior section of a 51 cm diameter sphere. Shaped Pierce and gate electrodes surround the source. ESQ aperture radii r_p (axis to rods), axial lengths ℓ , and typical rod-to-rod biases are: for Q1, $r_p = 12$ cm, $\ell = 31.04$ cm, and 201 kV; for Q2, $r_p = 12$ cm, $\ell = 45.77$ cm, and 346 kV; for Q3, $r_p = 10$ cm, $\ell = 47.75$ cm, and 301 kV; and for Q4, $r_p = 10$ cm, $\ell = 47.75$ cm, and 360 kV. Rods are axially separated from opposing endplates by 7.62 cm gaps, and endplates are 2.54 cm thick. Slit-scanner diagnostics are at the exit plane of the injector, with the first slit located 16 cm from the endplate of Q4. Further details of the injector geometry are presented in Refs. [1–3,12].

The ESQ injector is intrinsically 3d and WARP3d was extensively used in its design. Simulations and scaled experiments gave a thorough understanding of emittance growth due to aberrations arising from the so-called energy effect (i.e., changes in particle energy due to particles radially crossing equipotentials of the applied quadrupole field) and fourth-order error fields associated with the interdigitated quadrupole structure [1–3,5]. The full-scale ESQ injector constructed at LBNL achieved goals in beam energy, current, and emittance, and mid-pulse phase-space measures emerging from the injector were in qualitative agreement with WARP3d simulations carried out with space-charge limited injection and SOR field solutions including the detailed lattice geometry. However, slit-scanner measurements indicated a large degree of beam hollowing in the \perp charge density profile of the beam emerging from the injector [3,12]. In spite of this hollowing, WARP3d simulations and later experiments demonstrated that the beam could be manipulated with an ESQ matching section of seven quadrupoles, and the system has been successfully used as an experimental facility. Nevertheless, in a long transport channel, the excess self-field energy of the hollowed density profile would eventually thermalize, and the analytic theory [10] suggests that this can result in an unacceptable growth in emittance.

A sequence of WARP3d simulations were carried out to investigate possible causes of this beam hollowing. These included high-resolution, steady-state simulations with four-fold symmetry, up to $80 \times 80 \times 500$ grids ($dx = dy = 0.25 \text{ cm} \perp$ grid increments with $\pm 20 \text{ cm}$ grid bounds and longitudinal increment $dz = 0.5 \text{ cm}$), 5M particles, and SOR field solutions with the full conductor geometry. These subgrid field solutions were found using the experimentally measured potential biases and a lattice including shaped Pierce and gate electrodes, slit-scanner plates and electron guards, and ESQs formed from endplates and circular cross-section rods (with rod radii equal to $\frac{8}{9}$ the ESQ aperture radii r_p). Axial coordinates are chosen such that $z = 0$ corresponds to the source-axis intercept and the first slit diagnostic is at $z = 230.5 \text{ cm}$. Runs were carried out with both self-consistent space-charge limited injection from the source and planar injection of a SG beam. Planar injection conditions were set from rms equivalent beam measures (I , v_b , a , b , a' , b' , and $\varepsilon_{nx,ny}$) obtained from the self-consistent runs as follows. Dirichlet boundary conditions on the injection plane potential were found by loading the simulated line-charge $\lambda(z) = I/v_b(z)$ uniformly distributed in \perp planes within the envelope radii $a(z)$ and $b(z)$ and carrying out an SOR fieldsolve in the full geometry. Then the equivalent beam measures at the plane were injected as a SG distribution. Steady-state solutions were found by carrying out infrequent, computationally expensive, field-solves as the particles are advanced to fill the grid (timestep dt , with $v_b dt < dz$ at the injector exit), continuing till a steady solution (measured by the emittance) is found. (Some alternative iterative methods similar to those employed in the EGUN code [13] were numerically unstable in this AG geometry.) Typical runs are advanced 1.5–2.5 particle filling times on the grid with fieldsolves first taken as a reference particle reaches each ESQ entrance/exit and axial midpoint, and then more frequently till convergence was reached. Because the $\tau = 1 \mu\text{s}$ pulse is much longer than the injector, this steady-state solution represents the mid-pulse beam.

The WARP3d simulations suggest that injected beams with smooth density profiles result in only small amounts of beam hollowing at the exit plane

of the injector. Self-consistent diode simulations with WARP3d and EGUN are in good agreement with the experimentally measured current, suggesting that electrons are not being drawn into the ion-beam distribution. Provided the edge of the beam was well-resolved, typical emittance growth from the source to the injector exit was consistent with the experimental exit-plane measurements and a reasonable range of simulated values off the source, from $\varepsilon_{nx,ny} \sim 0.3 \text{ mm mrad}$ (\sim thermal source limit) to $\varepsilon_{nx,ny} \sim 1.0 \text{ mm mrad}$. Negligible differences were found between runs with all nonlinear applied field components removed (external linear focus and accelerative field components applied via multipole moments and conductors grounded), and runs with full field models. Also, runs with and without image charges (conductors removed and applied fields imposed via multipole moments) showed little difference. Likewise, runs with scaled beams (i.e., particle loads with $x_\perp \rightarrow \alpha x_\perp$, $v_\perp \rightarrow \alpha v_\perp$, $I \rightarrow \alpha^2 I$, and $\varepsilon_{nx,ny} \rightarrow \alpha^2 \varepsilon_{nx,ny}$ and $\alpha < \frac{1}{2}$) showed little change. Together, these results suggest that nonlinear applied fields, image-charge forces, and manifestations of the energy effect play, at most, a secondary role in the experimentally observed hollowing. However, certain simulations that included an error in the self-consistent injection algorithm (resulting in a distribution emerging from the diode with a highly peaked charge density near $r = 0$ and T_\perp increasing with r) produced a hollowed beam at the injector exit with features qualitatively similar to the experimental hollowing. This suggested the need to explore source perturbations.

The need for both high-resolution and good statistics in the present analysis render a systematic study of perturbations problematic with a 3d PIC code due to computer time and memory restrictions. This motivated the development of reduced models that incorporate the essential physics of the ESQ injector, culminating with a WARPxy slice model. This two-dimensional model employed the full 3d applied field structure of the lattice imported via multipole moments from WARP3d field solutions. The beam was initialized at the diode exit ($z = 29.5 \text{ cm}$) using both \perp beam slices imported from self-consistent WARP3d runs and rms equivalent “SG” distributions with and without

perturbations. Typical simulations employed a 128×128 grid (with and without four-fold symmetry, ± 10 cm bounds, and $dx = dy = 0.078$ cm), 1M particles, and step size $ds = 0.5$ cm. A comparison of beam envelope radii obtained in a typical WARPxy simulation and a self-consistent WARP3d simulation is shown in Fig. 4. These similar envelope evolutions ensure that similar applied field nonlinearities and space-charge forces are experienced in the two models. Moreover, similar emittance evolution and characteristic \perp phase-space distortions were observed in the WARPxy and WARP3d simulations. These results led us to believe that this reduced slice model with no axial self-fields could be used to economically investigate potentially problematic sensitivities to perturbations. In Fig. 4, note the presence of a pronounced beam neck (small cross-sectional area πab) in Q2. This neck is a general feature of injector operating points analyzed experimentally. High-resolution slice simulations with an initial SG beam suggest the presence of only a small surface mode at the beam edge-radius with insufficient amplitude to account for the experimental hollowing.

To access the effect of systematic source and diode errors, various classes of systematic perturba-

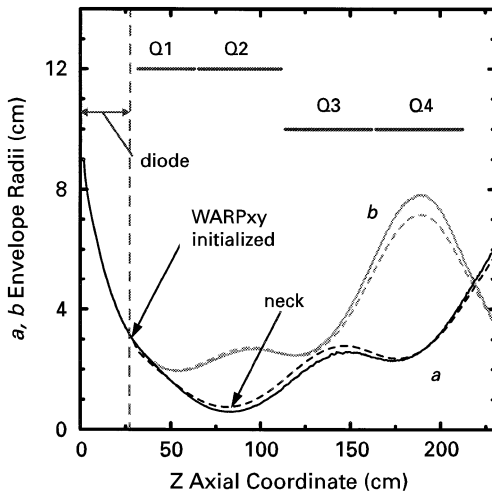


Fig. 4. Beam envelope comparisons of rms-radii a (black) and b (grey) obtained from self-consistent WARP3d (solid) and reduced WARPxy (dashed) simulations. Aperture radii and axial extents of the ESQs are indicated.

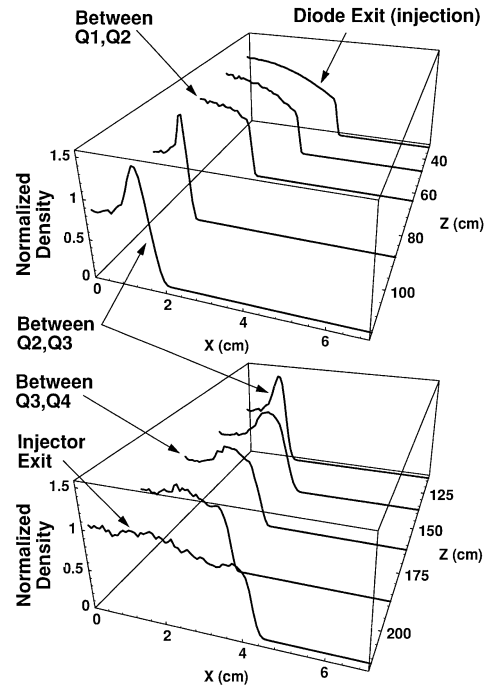


Fig. 5. Normalized charge density evolution along the x -axis for an initial large-amplitude \perp perturbation that is peaked on-axis.

tions were studied with the slice simulations. A typical evolution of an initial, large-amplitude density perturbation is shown in Fig. 5 in terms of the density evolution along the x -axis (evolution along the y -axis is similar). The initial perturbed beam is rms-equivalent to a 3d self-consistent run, has uniform kinetic temperature ($T_{\perp} = \text{const.}$), and a charge density profile that is constant on elliptical surfaces of constant $\eta^2 = (x/Fa)^2 + (y/Fb)^2$, parabolically decreasing $\propto 1 + (1 - h)\eta^2/h$ from on-axis ($\eta = 0$) to a value $1/h$ times the on-axis value at the beam edge ($\eta = 1$). Here, $F \equiv [(3 + 3h)/(4 + 2h)]^{1/2}$, and the evolution is shown for hollowing factor $h = 2$. Note that the perturbation evolves rapidly in the beam neck, where space-charge forces are enhanced. The evolution has similarities to particular Gluckstern modes which describe the self-consistent evolution of normal mode perturbations on a KV beam [14]. Surprisingly, the evolution shown in Fig. 5 is consistent with little emittance growth, with ε_{nx}

increasing from 0.5 to 0.54 mm mrad from initialization to the injector exit with oscillations of ~ 0.12 mm mrad. A range of initial perturbations in charge density (uniform with $h = 1$, peaked on-axis with $h > 1$, and hollowed on-axis with $h < 1$) and temperature (similarly uniform, peaked, and hollowed) showed similar behavior with rapid evolution in the neck and a sensitive dependence on initial launching conditions. For example, depending on the launching conditions and small parametric-induced changes in the envelope structure in the neck, the intricate wave evolution can result in an initial peaked density perturbation evolving to a hollowed, flat, or peaked perturbation on exiting the injector. Away from the neck, and in an extended AG lattice, these oscillations in density tend to appear and reappear, changing from hollowed to peaked and back. Depending on launching conditions and measurement phases, the perturbation can appear very different. Moreover, such collective oscillations can persist for many lattice periods inducing oscillations in emittance without steady growth. For the ESQ injector, only large-amplitude initial perturbations appear to be able to produce a degree of hollowing qualitatively consistent with experimental observations. Many large-amplitude perturbations also appear consistent with high beam quality at the injector exit. Evidently, the collective evolution of the perturbation has a slow thermalization rate and simulated changes in beam quality over the length of the injector are primarily associated with the nonlinear evolution of the wave.

In addition to systematic errors, source or diode problems can result in random errors of various type. To address this, a wide range of small (\perp extent), randomly distributed perturbations were studied with the slice simulations. A typical run is shown (with large perturbation strength for clarity) in Fig. 6. The initial x - y particle projection illustrates the graininess of the initial perturbed beam and the normalized charge density plots along the x - and y -axes at two axial locations illustrate the subsequent evolution. The initial beam was formed

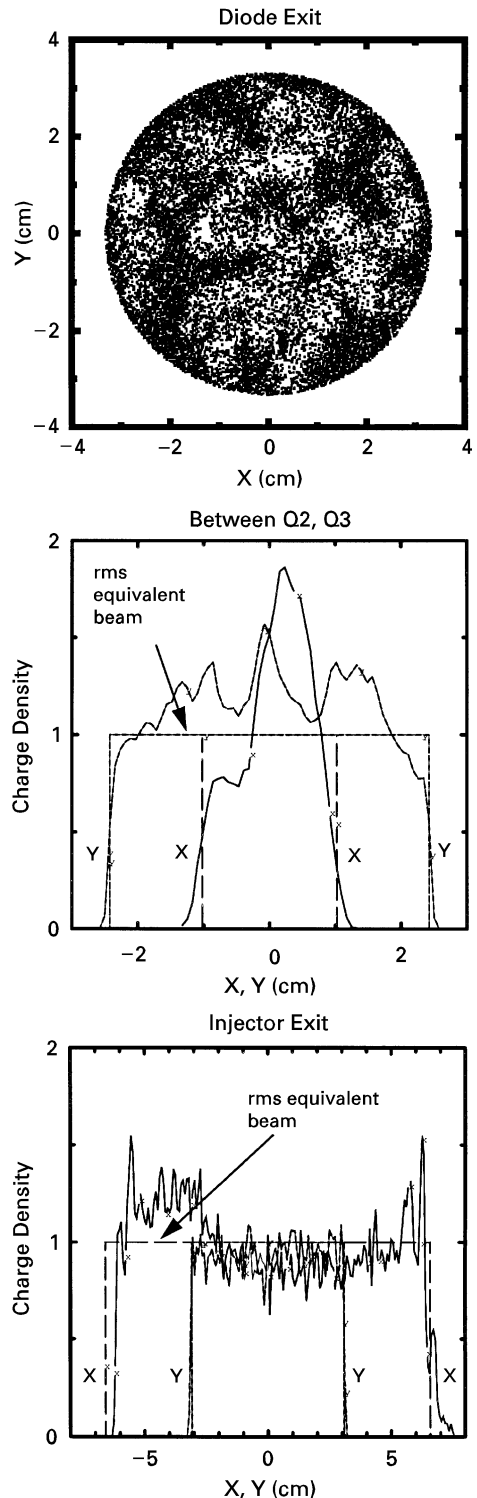


Fig. 6. Charge density evolution for initial \perp perturbations that are randomly distributed. The initial \perp particle distribution and two subsequent normalized charge density projections (with rms equivalent beam measures plotted) are shown.

by uniformly redistributing, throughout the unperturbed beam, $\frac{1}{2}$ the particles within 100 circular depletion zones with radii $0.1r_b$ that are applied sequentially and uniformly distributed throughout the \perp beam cross section.

Particle coordinate and velocities were adjusted to maintain rms-equivalency with the unperturbed beam and the transverse velocity spread is uniform [$T_{\perp}(x,y) = \text{const.}$]. Note that the perturbations tend to mix on propagation through the injector, becoming smoothed by the injector exit, resulting in a pronounced hollowing. Surprisingly, this evolution is consistent with small emittance growth, with ε_{nx} increasing from 0.5 to 0.6 mm mrad from initialization to the injector exit. A range of random perturbations were studied, including (in turn and in combination) variations in density, temperature (local T_{\perp} changes), and axial beam velocity, all with varying perturbation \perp size, amplitude, number, and pattern of distribution. No sensitivities were found that result in small-amplitude random perturbations growing and evolving to produce a large degree of hollowing consistent with experimental observations.

These simulation results suggest that an unanticipated, large-amplitude perturbation emerging from the diode is the most likely cause of the experimentally observed beam hollowing. Unanticipated electron or diagnostic problems could also be responsible. Since the experimental current measurements are in good agreement with ideal (uniform beam) space-charge-limited flow simulations with WARP3d and EGUN, and low beam emittance is measured at the exit of the injector, any perturbations are expected to be consistent with these strong constraints. The beam neck in Q2 also leads to a rapid wave evolution in this vicinity that depends sensitively on the detailed launching conditions of the initial perturbation emerging from the diode. This sensitivity is complicated by the inevitable differences between experiment and idealized simulations, and the multitude of possible initial perturbations in \perp phase-space. Present diagnostics are also limited to slit-scanner measurements at the injector exit, a point well removed from the diode and separated from it by the beam neck. These problems render difficult present comparisons between simulation and experiment to

uncover the relevant perturbations. Experiments are under way to measure the beam density and temperature profiles emerging from the diode. Also, ESQ voltages will be adjusted to mitigate the beam neck in Q2. It is anticipated that new simulations can be carried out with the resulting data to better characterize the beam evolution and thereby identify any relevant diode perturbation. Understanding and controlling such effects could be crucial to the ESQ injector concept and other injectors with similar high-current hot-plate sources. First principles PIC simulation of source perturbations consistent with overall space-charge-limited emission may require practical materials knowledge along with theory and modeling techniques beyond what is presently available, rendering such simulations challenging. Nevertheless, if measurements indicate source difficulties, this problem must be addressed. Simulations will also be carried out to evaluate characteristics of various electron effects.

5. Conclusions

The WARP PIC code has become a valuable tool in support of HIF experiments at LLNL and LBNL. Here, present WARP modeling capabilities were illustrated in the analysis of two experiments. First, simulations were carried out on the evolution of \perp beam emittance in a beam-bending experiment at LLNL. These simulations demonstrate that the emittance in the plane of the bend is a sensitive function of the dispersion. Results suggest that near-term experimental measurements of the emittance should be able to indirectly bound the spread in axial beam velocity emerging from the diode. Second, simulations were carried out on a driver scale injector at LBNL to search for the cause of experimentally observed beam hollowing. An analysis of space-charge waves seeded by both systematic and random perturbations along with identified parametric sensitivities suggest that the hollowing may be due to source difficulties as opposed to instabilities. Both these studies suggest the need for further work to understand sources of intense ion beams – in terms of both characteristic velocity spreads and other perturbations. Careful studies involving the LLNL and LBNL experiments

and WARP simulations promise to increase our understanding on these topics of fundamental interest to HIF.

Acknowledgements

This research was performed under the auspices of the US Department of Energy at LLNL under contract W-7405-ENG-48.

References

- [1] See references in, S. Atzeni, R.A. Ricci (Eds.), Proc. Int. Symp. on Heavy Ion Inertial Fusion, Frascati, Italy, 25–28 May 1993, IL; Nuovo Cimento 106 (1993) 1429.
- [2] See references in, J.J. Barnard, T.J. Fessenden, E.P. Lee (Eds.), Proc. Int. Symp. on Heavy Ion Inertial Fusion, Princeton, NJ, USA, 6–9 September 1995; J. Fusion Eng. Des. 32–33 (1996) 1.
- [3] See references in, Proc. Int. Symp. on Heavy Ion Inertial Fusion, Heidelberg, Germany, 24–17 September 1997; Nucl. Instr. and Meth. (1998) these proceedings.
- [4] A. Friedman, D.P. Grote, Phys. Fluids B 4 (1992) 2203.
- [5] D.P. Grote, Three dimensional simulations of space charge dominated heavy ion beams with applications to inertial fusion energy, Ph.D. Dissertation, Lawrence Livermore Laboratory, publication UCRL-LR-119363, 1994, pp. 1–129.
- [6] D.P. Grote, I. Haber, A. Friedman, S.M. Lund, WARP3d, a three-dimensional PIC code for high-current ion-beam propagation developed for heavy-ion fusion, ICF Quarterly Report, Lawrence Livermore National Laboratory, publication UCRL-LR-105821-96-4, vol. 6, 1996, pp. 129–137.
- [7] S.M. Lund, On the 3D field structure of rectangular block permanent magnet lenses, Lawrence Livermore National Laboratory, Internal Group Note, HIF Note Number 96-10, 1996, pp. 1–38.
- [8] J.J. Barnard, H.D. Shay, S.S. Yu, A. Friedman, D.P. Grote, emittance growth in heavy ion recirculators, in: C.R. Hoffman (Ed.), Proc. 1992 Linear Accelerator Conf., AECL 10782, Ottawa, August 1992, pp. 229–231.
- [9] E.P. Lee, Nucl. Instr. and Meth. A 278 (1989) 178.
- [10] M. Reiser, Theory and Design of Charged Particle Beams, McGraw-Hill, New York, 1994.
- [11] J.J. Barnard Implications of pulser voltage ripple, Lawrence Livermore National Laboratory, internal group note, HIF Note Number 96-12, 1996, pp. 1–12.
- [12] S. Yu, S. Eylon, E. Henestroza, D. Grote, Space-charge dominated heavy ion beams in electrostatic quadrupole accelerators, in: S.Y. Lee (Ed.), Space Charge Dominated Beams and Applications of High Brightness Beams, Bloomington, IN, USA, 10–13 October 1995; AIP Conf. Proc., vol. 377, American Institute of Physics, New York, 1996, pp. 134–144.
- [13] W.B. Herrmannsfeldt, EGUN – an electron optics and gun design program, Technical Report 331, Stanford Linear Accelerator Center, 1988.
- [14] R.L. Gluckstern, W.-H. Cheng, H. Ye, Phys. Rev. Lett. 75 (1995) 2835.